

Inertia drives concentration-wave turbulence in swimmer suspensions

Purnima Jain,¹ Navdeep Rana,² Sriram Ramaswamy,³ and Prasad Perlekar^{1,*}

¹Tata Institute of Fundamental Research, Hyderabad, India

²Max Planck Institute for Dynamics and Self-Organization (MPIDS), D-37077 Göttingen, Germany

³Indian Institute of Science, Bangalore, India

We discover an instability mechanism in suspensions of self-propelled particles that does not involve active stress. Instead, it is driven by a subtle interplay of inertia, swimmer motility, and concentration fluctuations, through a crucial time lag between the velocity and the concentration field. The resulting time-persistent state seen in our high-resolution numerical simulations consists of self-sustained waves of concentration and orientation, transiting from regular oscillations to wave turbulence. We analyze the statistical features of this active turbulence, including an intriguing connection to the Batchelor spectrum of passive scalars.

Hydrodynamic theories of active matter [1–4] are remarkably successful in predicting and accounting for the complex spatiotemporal flows arising in suspensions of motile organisms. The dominance of viscosity over inertia in the case of microbial systems leads to a seemingly inexorable instability due to active stresses for bulk Stokesian systems [5], mitigated by a solid substrate [6, 7] or, more subtly, a fluid interface [8].

Studies focusing on mesoscale swimmers have made a strong case for investigating active suspensions in realms where inertial effects are significant [9–11]. We showed recently [10, 12] that in a suspension with mass density ρ , when concentration fluctuations are ignored, the squared dimensionless ratio $R = \rho v_0^2 / \sigma_a$ of the swimming speed v_0 to the invasion speed $\sqrt{\sigma_a / \rho}$ of active stresses controls the stability of the ordered state. Inertia thus stabilizes the suspension and long-range order is recovered in the regime where inertia dominates $R \gg 1$ [10, 12].

In this Letter we uncover a manifestation of the roles of activity *and* inertia with a character qualitatively distinct from that hitherto explored in active hydrodynamics. We model the dynamics of a swimmer suspension using a continuum framework [5] for the active particle concentration $c(\mathbf{x}, t)$, the hydrodynamic velocity $\mathbf{u}(\mathbf{x}, t)$, and the vector orientational order parameter $\mathbf{p}(\mathbf{x}, t)$.

We work at $R \gg 1$, where inertia has eliminated the instability due to active stresses, and activity enters only through motility. The equations of motion [2, 5, 10, 12–14] read [15]

$$\rho \partial_t \mathbf{u} = -\nabla P + \mu \nabla^2 \mathbf{u} + \nabla \cdot \boldsymbol{\Sigma}, \quad (1)$$

$$\partial_t \mathbf{p} + (\mathbf{u} + v_0 \mathbf{p}) \cdot \nabla \mathbf{p} = \lambda \mathbf{S} \cdot \mathbf{p} + \boldsymbol{\Omega} \cdot \mathbf{p} + \Gamma \mathbf{h}, \quad \text{and} \quad (2)$$

$$\partial_t c + \nabla \cdot [(\mathbf{u} + v_1 \mathbf{p})c] = D \nabla^2 c, \quad (3)$$

where ρ is the constant suspension density and the pressure P enforces the incompressibility constraint $\nabla \cdot \mathbf{u} = 0$. v_0 and v_1 are the speeds of self-advection and -propulsion, the tensors \mathbf{S} and $\boldsymbol{\Omega}$ are the symmetric and antisymmetric part of the velocity gradient tensor, and λ denotes the flow alignment parameter [16, 17]. The collective orientational mobility Γ ($\sim 1/\mu$ in molecular systems, μ being the dynamic viscosity) governs the relaxational response

of \mathbf{p} to the molecular field \mathbf{h} . The reversible thermodynamic stress is $\boldsymbol{\Sigma} \equiv -\lambda_+ \mathbf{h} \mathbf{p} - \lambda_- \mathbf{p} \mathbf{h}$ with $\lambda_{\pm} \equiv (\lambda \pm 1)/2$ [10, 18, 19]. $\mathbf{h} \equiv -\delta F / \delta \mathbf{p}$ is the molecular field conjugate to \mathbf{p} , derived from the free energy functional

$$F = \int d\mathbf{x} \left[-\frac{a(c)}{2} |\mathbf{p}|^2 + \frac{1}{4} |\mathbf{p}|^4 + \frac{K}{2} |\nabla \mathbf{p}|^2 + E \mathbf{p} \cdot \nabla c \right]. \quad (4)$$

We choose $a(c) = a \tanh mc$, with $a < 0$ and $m > 0$ [20]. This ensures the existence of two steady state homogeneous solutions: the disordered state ($\mathbf{u} = 0, c = 0, \mathbf{p} = 0$), and an orientationally ordered state ($\mathbf{u} = 0, c = c_0, \mathbf{p} = \sqrt{a(c_0)}$) with $c_0 > 0$.

In (4), a single Frank constant K penalizes the spatial deformations in \mathbf{p} [21, 22] and the parameter E governs the alignment of \mathbf{p} with respect to ∇c . This term, analogous to the flexoelectric coupling in liquid crystals [23], is unique to polar fluids because it breaks the $\mathbf{p} \rightarrow -\mathbf{p}$ symmetry [24]. As we are interested in the physics at moderately low Reynolds numbers $\text{Re} \lesssim 1$, we have ignored the advective nonlinearity in (1). We re-emphasize that we have ignored the active stresses, as we are interested in the inertia-dominated regime $R \gg 1$.

We present a novel inertial instability driven by motility and concentration fluctuations that disrupt the orientationally ordered state even without active stresses. Following a linear stability analysis, we propose a minimal 1D model where we extract essential terms from the full hydrodynamic equations to describe the physical mechanism of the instability. Finally, using high-resolution numerical simulations in two dimensions, we unveil three distinct states that arise from this new hydrodynamic instability: (1) Traveling waves, (2) a crossover regime featuring coexisting waves and defects, and (3) concentration-wave turbulence.

Linear Stability Analysis – The evolution of infinitesimal perturbations $\phi \equiv (\delta c, \delta p_y, \delta u_x)$ to the ordered steady state ($c = c_0, \mathbf{p} = p_0 \hat{x}, \mathbf{u} = \mathbf{0}$) is governed by the linear system $\partial_t \phi_{\mathbf{q}}(t) + \mathbf{M}(\mathbf{q}) \cdot \phi_{\mathbf{q}}(t) = 0$, where $\phi \equiv \phi_{\mathbf{q}} e^{i(\mathbf{q} \cdot \mathbf{x} - \omega t)}$. For pure splay perturbations ($\mathbf{q} = q \hat{y}$),

we have [15]

$$\mathbf{M}(\mathbf{q}) = \begin{pmatrix} Dq^2 & iv_1c_0q & 0 \\ i\Gamma E q & \Gamma K q^2 & -ip_0\lambda_-q \\ \lambda_-Ep_0q^2/\rho & -ip_0Kq^3\lambda_-/\rho & \mu q^2/\rho \end{pmatrix}. \quad (5)$$

In the hydrodynamic limit ($q \rightarrow 0$), up to $\mathcal{O}(q^2)$, we obtain the following dispersion relation [25]

$$\omega(q) = \pm q \sqrt{\Gamma E v_1 c_0} + \frac{iq^2}{2} \left[\frac{p_0^2 \lambda_-^2}{\Gamma \rho} - (D + \Gamma K) \right], \quad (6)$$

which is valid for

$$q \ll \frac{2\Gamma\rho\sqrt{\Gamma E v_1 c_0}}{\sqrt{3} [3\lambda_-^2 p_0^2 + \Gamma(2\mu - \rho D - \Gamma K \rho)]}. \quad (7)$$

A novel $\mathcal{O}(q^2)$ instability emerges for $E > 0$ when $\Gamma\rho(D + \Gamma K) < \lambda_-^2 p_0^2$. At $\mathcal{O}(q)$ we observe the familiar Toner-Tu waves propagating with the speed $\sim \sqrt{\Gamma E v_1 c_0}$ [26, 27]. Although the coefficient E cancels out from the second term in (6), inertia, concentration terms in the reversible stresses and the order parameter equation, and the self-propulsion term in the concentration equation are all crucial for the instability. In the absence of any one of these couplings, the system (5) is linearly stable [15].

When $E < 0$, on the other hand, we observe an unstable mode with growth rate of $\mathcal{O}(q)$, that persists in the absence of the reversible stresses and arises even without the hydrodynamic velocity field. This instability is simply an extension of motility-induced phase separation (MIPS), well-known for dry active matter [28–30] and not relevant to our present work.

Instability mechanism – To understand the mechanism of the novel $\mathcal{O}(q^2)$ instability, we propose a minimal 1D model keeping only the essential terms from the full hydrodynamic equations that exhibit linear dispersion relations identical to (6). We restrict our analysis to gradients in the transverse direction $\hat{\mathbf{y}}$ with respect to the ordering direction $\hat{\mathbf{x}}$. The incompressibility condition, $\partial_x u_x + \partial_y u_y = 0$, yields $\partial_y u_y = 0$, which allows us to set u_y as a constant, chosen to be zero. For clarity, we denote $u_x = v$ and $p_y = p$ in the remaining of this section. Consequently, the minimal 1D hydrodynamic equations for the variables $v(y, t)$, $p(y, t)$, and $c(y, t)$ are

$$\begin{aligned} \rho \partial_t v &= \mu \partial_y^2 v + \lambda_- p_0 E \partial_y^2 c, \\ \partial_t p &= \lambda_- p_0 \partial_y v - \Gamma b p^3 + \Gamma K \partial_y^2 p - \Gamma E \partial_y c, \text{ and} \\ \partial_t c &= -v_1 \partial_y (pc) + D \partial_y^2 c. \end{aligned} \quad (8)$$

We now show that inertia is essential for the instability. Consider first the Stokesian regime, where the balance of the viscous and reversible stresses instantly determines the velocity field as

$$\mu \partial_y^2 v \approx -\lambda_- p_0 E \partial_y^2 c. \quad (9)$$

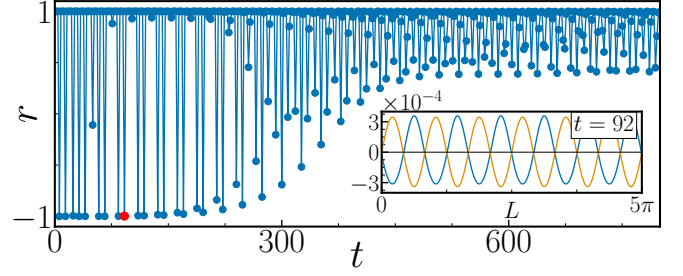


FIG. 1. Pearson’s correlation coefficient $r(t)$ at early times oscillates between -1 and 1 , implying varying temporal lag between v and c . Inset: Velocity v (orange) and concentration fluctuation $c - \bar{c}$ (blue) profiles at $t = 92$ (marked by red dot in the r plot) during the onset of instability. v and c are out-of-phase, which is crucial for the instability.

After eliminating v from the p equation we get

$$\partial_t p = -(\Gamma E + \lambda_-^2 p_0^2 E / \mu) \partial_y c - \Gamma b p^3 + \Gamma K \partial_y^2 p, \quad (10)$$

where the concentration field couples to the order parameter via the pressure-like term $\partial_y c$, with an additional contribution arising from the reversible stresses that accelerate the relaxation rate of the splay waves, rendering the system *stable*.

Inertia introduces a crucial temporal lag between velocity and concentration that can negate the stability of the splay waves. While concentration attempts to relax, velocity may, at certain times, counteract this relaxation process. This out-of-phase interaction between velocity and concentration, driven by inertia, gives rise to the novel instability under consideration. To quantify our observations, we numerically integrate (8) for $E = 0.2$ and plot the time evolution of Pearson’s correlation coefficient $r(t)$ [15, 31] between the velocity and concentration fields in Fig. 1.

Direct Numerical Simulations – To quantify the non-equilibrium steady states emerging from the instability, we numerically integrate (1) to (3) on a periodic square domain of length $L = 10\pi$ discretized with $N^2 = 1024^2$ points [15]. We use the streamfunction-vorticity formulation for the numerical integration of (1) [32]. The spatial derivatives are evaluated using a fourth-order centered finite-difference scheme, and a second-order Adams Bashforth scheme is used for time integration. In what follows, we study the statistically steady states with varying E while keeping other parameters fixed ($\rho = 1$, $\mu = 0.1$, $\Gamma = 1$, $D = 10^{-4}$, $K = 10^{-3}$, $\lambda = 0.1$, $v_1 = v_0 = 0.1$, and $c_0 = 1$). Fig. 2 shows the snapshots of the concentration field and streamlines of the order parameter field in the steady-state for various values of E . As E increases, disorder sets in and fluctuations in the concentration field decrease. We quantify the same in Fig. 3, which shows the plot of the average order $|\langle \mathbf{p} \rangle|$, the variance in concentration $\sigma_c^2 \equiv \langle c^2 \rangle - \langle c \rangle^2$, and the kinetic energy density $\mathcal{K} \equiv \langle \mathbf{u}^2 / 2 \rangle$. Here, the angular brackets denote spatio-

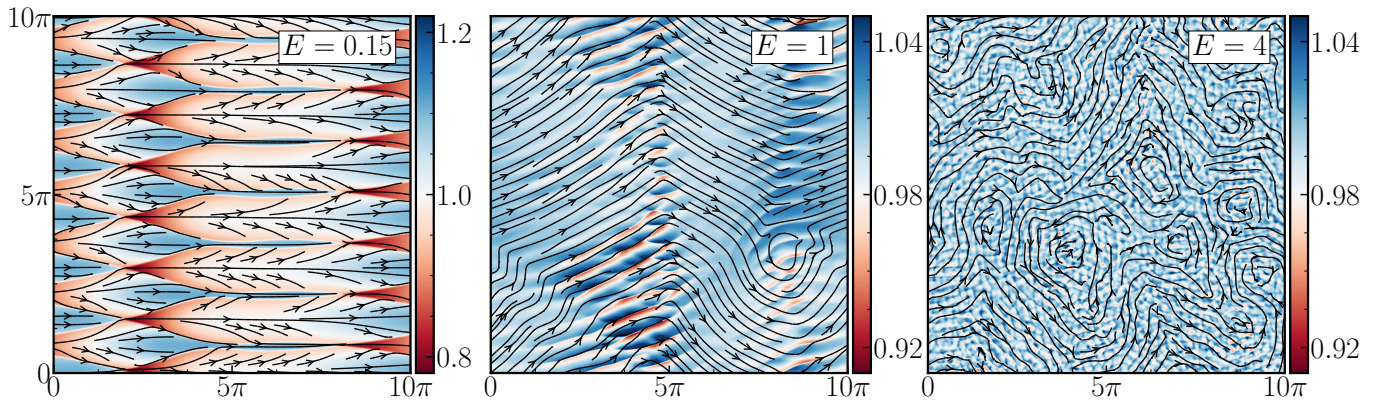


FIG. 2. Pseudocolor plot of the concentration superimposed with streamlines of the order parameter for different E . With increasing E , disorder sets in and the strength of concentration fluctuations diminishes. The system transitions from travelling waves at small $E \leq 0.8$ to a crossover phase at intermediate $0.8 < E < 4$ and then finally to concentration wave turbulence at large $E \gtrsim 4$.

temporal averaging in the steady state. Consistent with the snapshots, $|\langle \mathbf{p} \rangle|$ decreases as E increases. Yet, even for the largest $E = 6$ simulated, partial ordering persists and we find $|\langle \mathbf{p} \rangle| \approx 0.27 > 0$. For $E \leq 0.8$ and $E > 2$, \mathcal{K} increases monotonically, whereas σ_c^2 decreases. In between, we find a short cross-over region where all of $|\langle \mathbf{p} \rangle|$, σ_c^2 , and \mathcal{K} exhibits large fluctuations as marked by significant error bars in Fig. 3. A careful inspection of Figs. 2 and 3, and other quantifiers shows the presence of three distinct regimes which we now describe.

I. *Travelling waves* – For $E \leq 0.8$, we observe travelling waves. Fig. 2 ($E = 0.15$) shows a typical realization of the concentration field in this regime. In Fig. 4(a), we plot $|\nabla c|$ for $E = 0.15$ [15] and identify with iso $|\nabla c| = 0.5$ contours, two wavefronts moving orthogonal to each other in the direction $-\nabla c/|\nabla c|$. Intriguingly, the wavefronts behave like solitons, they move at a constant speed and their shape remains preserved as they pass through each other. By tracking the wavefronts, we evaluate their speed U_E and the wavelength ℓ_E which are plotted in Fig. 4(b). Consistent with the dimensional analysis, we find $U_E \sim \sqrt{\Gamma E v_1 c_0}$ and $\ell_E \sim \mu/(\rho\sqrt{\Gamma E v_1 c_0})$.

II. *The crossover phase* – For $0.8 < E < 4$, waves and defects coexist. The wave trains discussed in the previous section are destabilized, and we observe the spontaneous appearance of vortical structures in the order parameter field (See $E = 1$ in Fig. 2). Consistent with the large error bars in σ_c^2 in Fig. 3(a), the plot of $\overline{c^2(t)} = (1/L) \int c^2 dx$ in the steady state shows large fluctuations [15]. Small values of $\overline{c^2(t)} - \overline{c(t)}^2 < 10^{-4}$ correspond to the nearly homogeneous c and nearly ordered \mathbf{p} field [15].

III. *Concentration-wave turbulence* ($E > 4$) – To resolve large and small-scale structures in the turbulent regime, we perform large scale simulations at $L = 100\pi$ with a grid resolution of $N^2 = 8192^2$ while keeping other parameters fixed. The time evolution of the concentra-

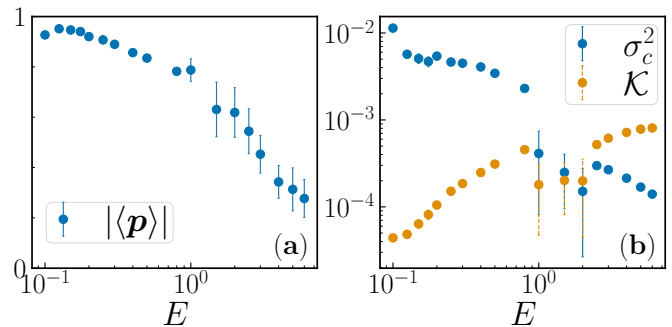


FIG. 3. Plot of (a) average order $|\langle \mathbf{p} \rangle|$, (b) kinetic energy \mathcal{K} , and the concentration variance σ_c^2 versus E . With increasing E , σ_c^2 and $|\langle \mathbf{p} \rangle|$ decrease and \mathcal{K} increases. All the quantities show large fluctuations in the crossover phase as marked by error bars.

tion field shows the presence of traveling concentration waves, and the order parameter streamlines show complex spatiotemporal structures [See Fig. 2 ($E = 4$) and the movie]. These concentration waves resemble that observed in Regime I and their wavelength is $\sim \ell_E$.

We characterize the turbulent regime using the power spectrum of the order parameter, concentration, and velocity fields i.e.,

$$\mathcal{E}_{\mathbf{p}}(q) \equiv \sum_{\mathbf{k}} |\hat{\mathbf{p}}_{\mathbf{k}}|^2, \quad \mathcal{E}_c(q) \equiv \sum_{\mathbf{k}} |\hat{c}_{\mathbf{k}}|^2, \quad \text{and} \quad \mathcal{E}_{\mathbf{u}}(q) \equiv \sum_{\mathbf{k}} |\hat{\mathbf{u}}_{\mathbf{k}}|^2, \quad (11)$$

where $\hat{\cdot}_{\mathbf{k}}$ denotes the Fourier coefficient of the wavenumber \mathbf{k} and $\sum'_{\mathbf{k}}$ implies a sum over all Fourier modes that satisfy $q - \pi/L \leq |\mathbf{k}| < q + \pi/L$. In Fig. 5 we plot the time averaged $\mathcal{E}_{\mathbf{p}}(q)$, $\mathcal{E}_c(q)$, and $\mathcal{E}_{\mathbf{u}}(q)$ in the steady state and observe a clear signature of concentration waves — all the spectra show a large- q peak around $q \sim 2\pi/\ell_E$. $\mathcal{E}_{\mathbf{p}}(q)$ and $\mathcal{E}_{\mathbf{u}}(q)$ show a small- q peak at $q \sim q_*$, which is

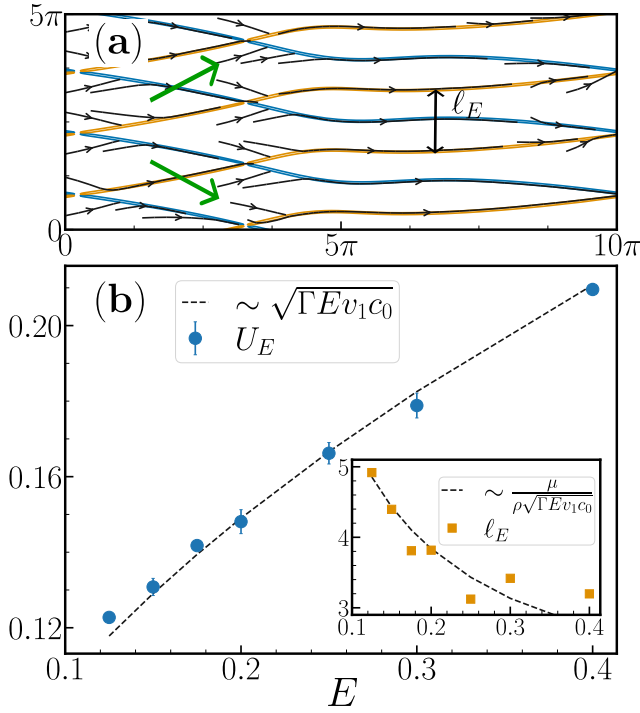


FIG. 4. (a) Iso-contours of $|\nabla c| = 0.5$ superimposed on streamlines of \mathbf{p} (black lines) for $E = 0.15$. Contours with $\nabla c \cdot \hat{y} > 0 (< 0)$ are drawn with orange (blue) lines. Solid Green arrows show the direction in which the wavefront travels. (b) Wave speed U_E and (Inset) distance between wavefronts ℓ_E versus E . (Black dashed line) Prediction based on dimensional analysis $U_E \sim \sqrt{\Gamma E v_1 c_0}$ and $\ell_E \sim \mu/(\rho\sqrt{\Gamma E v_1 c_0})$.

inversely proportional to the size of a typical large eddy. $\mathcal{E}_p(q)$ has two power law regimes around q_* . For $q \ll q_*$, we obtain equipartition spectrum $\mathcal{E}_p(q) \sim q$, indicating that the fluctuations in the order parameter field are uncorrelated. In the regime $q_* < q < 2\pi/\ell_E$, we find a modified Porod's scaling $\mathcal{E}_p(q) \sim q^{-(1+d_2)}$, where d_2 is the correlation dimension which characterizes the clustering of the topological defects over these length scales [12, 15]. Remarkably, the profile of the spectrum and the exponents are close to the models of bacterial turbulence, where activity is modeled as a small-scale energy injection mechanism [33].

At large length scales ($q \ll q_*$), $\mathcal{E}_p(q) \gg \mathcal{E}_u(q)$, thus the concentration field is primarily advected by random fluctuations of the order parameter. As the Schmidt number $Sc \equiv \mu/(\rho D) \gg 1$, we observe Batchelor scaling $\mathcal{E}_c(q) \sim q^{-1}$ for $q < q_*$, establishing a nice connection to the phenomenology of stochastically advected passive scalars [34, 35]. Finally, in Fig. 5(b), we account for the velocity spectrum by balancing viscous dissipation with the contribution of the alignment interaction term in the

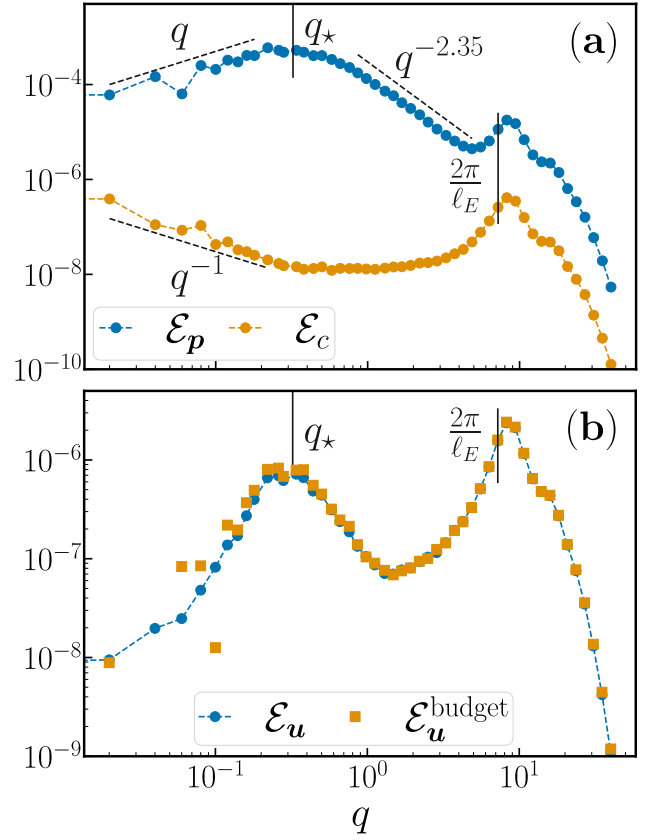


FIG. 5. (a) Plot of the order parameter spectra $\mathcal{E}_p(q)$, the concentration spectra $\mathcal{E}_c(q)$, and (b) Plot of the kinetic energy spectra $\mathcal{E}_u(q)$ for $E = 4$. All spectra show a peak at $2\pi/\ell_E$. $\mathcal{E}_p(q)$ and $\mathcal{E}_u(q)$ show a small- q peak at q_* . $\mathcal{E}_p(q) \sim q^{-(1+d_2)}$ in the regime $q_* < q < 2\pi/\ell_E$ where $d_2 = 1.35$ is the correlation dimension of the clustering of topological defects. $\mathcal{E}_c(q)$ shows Batchelor scaling for $q < q_*$. Finally, the dominant balance (12) shows excellent agreement with $\mathcal{E}_u(q)$. $q_* \sim 0.32$, and $\ell_E \sim 0.87$.

reversible stress $\Sigma_E = \lambda_+ E(\nabla c)\mathbf{p} + \lambda_- \mathbf{p} E \nabla c$. We have

$$\mu q^2 \langle |\hat{\mathbf{u}}_q|^2 \rangle_t \approx \frac{\langle \hat{\mathbf{u}}_q^* \cdot \hat{\mathbf{f}}_q + \hat{\mathbf{f}}_q^* \cdot \hat{\mathbf{u}}_q \rangle_t}{2}, \quad (12)$$

where $\langle \cdot \rangle_t$ implies time averaging in the steady state, $\hat{\mathbf{f}}_q = \mathcal{P} \cdot (i\mathbf{q} \cdot \hat{\Sigma}_E)$, and \mathcal{P} is the projection operator. The energy spectrum $\mathcal{E}_u^{\text{budget}}$ obtained from this dominant balance analysis is in excellent agreement with $\mathcal{E}_u(q)$.

Conclusions — We identify a novel inertial instability in an active suspension of polar particles. Crucially, unlike earlier studies [5, 10, 12, 36], active stresses are not essential for the instability. We use extensive numerical simulations to investigate the steady-state properties of the suspension by varying the strength of the coupling between the order parameter and the concentration field. We identify three regimes: I) Travelling waves, II) cross-over phase, and III) Concentration wave turbulence.

PJ and PP acknowledge support from the Department of Atomic Energy (DAE), India under Project Identifi-

fication No. RTI 4007, and DST (India) Project Nos. MTR/2022/000867, and DST/NSM/R&D HPC Applications/Extension/2023/08. SR gratefully acknowledges a J C Bose Fellowship of the SERB, India, and thanks the Isaac Newton Institute for Mathematical Sciences, Cambridge, for support and hospitality during the programme Anti-diffusive dynamics: from sub-cellular to astrophysical scales where work on this paper was undertaken, supported by EPSRC grant no EP/R014604/1. All the simulations are performed using the HPC facility at TIFR Hyderabad.

* perlekar@tifrh.res.in

- [1] S. Ramaswamy, *Annu. Rev. Condens. Matter Phys.* **1**, 323 (2010).
- [2] M. C. Marchetti, J. F. Joanny, S. Ramaswamy, T. B. Liverpool, J. Prost, M. Rao, and R. A. Simha, *Rev. Mod. Phys.* **85**, 1143 (2013).
- [3] S. Ramaswamy, *Nat Rev Phys* **1**, 640 (2019).
- [4] R. Alert, J. Casademunt, and J.-F. Joanny, *Annual Review of Condensed Matter Physics* **13**, 143 (2022).
- [5] R. A. Simha and S. Ramaswamy, *Phys. Rev. Lett.* **89**, 058101 (2002).
- [6] A. Maitra, P. Srivastava, M. C. Marchetti, S. Ramaswamy, and M. Lenz, *Phys. Rev. Lett.* **124**, 028002 (2020).
- [7] N. Sarkar, A. Basu, and J. Toner, *Phys. Rev. Lett.* **127**, 268004 (2021).
- [8] A. Maitra, *Nat. Phys* **19**, 733–740 (2023).
- [9] D. Klotsa, *Soft Matter* **15**, 8946 (2019).
- [10] R. Chatterjee, N. Rana, R. A. Simha, P. Perlekar, and S. Ramaswamy, *Phys. Rev. X* **11**, 031063 (2021).
- [11] N. J. Derr, T. Dombrowski, C. H. Rycroft, and D. Klotsa, *Journal of Fluid Mechanics* **952**, A8 (2022).
- [12] N. Rana, R. Chatterjee, S. Ro, D. Levine, S. Ramaswamy, and P. Perlekar, Defect turbulence in a dense suspension of polar, active swimmers (2023), arXiv:2305.15197 [cond-mat.soft].
- [13] M. E. Cates and E. Tjhung, *J. Fluid Mech.* **836**, P1 (2018).
- [14] K. Kruse, J. F. Joanny, F. Jülicher, J. Prost, and K. Sekimoto, *Eur. Phys. J. E* **16**, 5 (2005).
- [15] Supplemental Material available at ???. It includes details of the linear stability analysis, Pearson’s correlation, correlation dimension of the topological defects, and description of the movies.
- [16] D. Forster, *Phys. Rev. Lett.* **32**, 1161 (1974).
- [17] R. G. Larson, *The Structure and Rheology of Complex Fluids*, Topics in Chemical Engineering (Oxford University Press, New York, 1999).
- [18] P. G. de Gennes and J. Prost, *The Physics of Liquid Crystals*, 2nd ed., Oxford Science Publications No. 83 (Clarendon Press ; Oxford University Press, Oxford ; New York, 1993).
- [19] S. Chandrasekhar, *Liquid Crystals*, 2nd ed. (Cambridge University Press, Cambridge [England] ; New York, NY, USA, 1992).
- [20] In our simulations, $a = 1/10$ and $m = 10$.
- [21] F. C. Frank, *Discuss. Faraday Soc.* **25**, 19 (1958).
- [22] C. Oseen, *Transactions of the Faraday Society* **29**, 883 (1933).
- [23] R. B. Meyer, *Phys. Rev. Lett.* **22**, 918 (1969).
- [24] W. Kung, M. Cristina Marchetti, and K. Saunders, *Phys. Rev. E* **73**, 031708 (2006).
- [25] On rescaling the length by $\mu/\rho\sqrt{\Gamma E v_1 c_0}$ and time by $\mu/\rho(\Gamma E v_1 c_0)$, we obtain a non-dimensional form of the dispersion relation that does not explicitly depend on E [15].
- [26] J. Toner and Y. Tu, *Phys. Rev. Lett.* **75**, 4326 (1995).
- [27] J. Toner and Y. Tu, *Phys. Rev. E* **58**, 4828 (1998).
- [28] M. E. Cates and J. Tailleur, *Annu. Rev. Condens. Matter Phys.* **6**, 219 (2015).
- [29] J. Bialké, H. Löwen, and T. Speck, *Europhysics Letters* **103**, 30008 (2013).
- [30] D. Geyer, D. Martin, J. Tailleur, and D. Bartolo, *Phys. Rev. X* **9**, 031043 (2019).
- [31] W. H. Press, S. A. Teukolsky, W. T. Vetterling, and B. P. Flannery, *Numerical Recipes 3rd Edition: The Art of Scientific Computing*, 3rd ed. (Cambridge University Press, 2007).
- [32] P. Perlekar and R. Pandit, *New J. Phys.* **11**, 073003 (2009).
- [33] H. H. Wensink, J. Dunkel, S. Heidenreich, K. Drescher, R. E. Goldstein, H. Lowen, and J. M. Yeomans, *Proceedings of the National Academy of Sciences* **109**, 14308 (2012).
- [34] G. K. Batchelor, *Journal of Fluid Mechanics* **5**, 113–133 (1959).
- [35] R. H. Kraichnan, *J. Fluid Mech.* **64**, 737 (1974).
- [36] L. Giomi and M. C. Marchetti, *Soft Matter* **8**, 129 (2012).

Supplementary Material for Inertia drives concentration-wave turbulence in swimmer suspensions

Purnima Jain,¹ Navdeep Rana,² Sriram Ramaswamy,³ and Prasad Perlekar^{1,*}

¹*Tata Institute of Fundamental Research, Hyderabad, India*

²*Max Planck Institute for Dynamics and Self-Organization (MPIDS), D-37077 Göttingen, Germany*

³*Indian Institute of Science, Bangalore, India*

CONTENTS

I. Linear Stability Analysis	1
II. Numerical integration of the 1D equation and Pearson's correlation	3
III. Dispersion for the traveling waves	4
IV. Crossover-phase	4
V. Correlation dimension	5
VI. Description of the movies	5
References	6

I. LINEAR STABILITY ANALYSIS

We study the linear stability of equation(1-3) from main text about homogeneous ordered steady state ($\mathbf{u} = 0$, $\mathbf{p} = p_0\hat{x}$, $c = c_0$). The equations are

$$\rho\partial_t\mathbf{u} = -\nabla P + \mu\nabla^2\mathbf{u} + \nabla \cdot \Sigma, \quad (\text{S1})$$

$$\partial_t\mathbf{p} + (\mathbf{u} + v_0\mathbf{p}) \cdot \nabla\mathbf{p} = \lambda\mathbf{S} \cdot \mathbf{p} + \mathbf{\Omega} \cdot \mathbf{p} + \Gamma\mathbf{h}, \text{ and} \quad (\text{S2})$$

$$\partial_t c + \nabla \cdot [(\mathbf{u} + v_1\mathbf{p})c] = D\nabla^2 c. \quad (\text{S3})$$

We choose monochromatic perturbations of the form

$$\phi \equiv \begin{pmatrix} \delta c \\ \delta p_y \\ \delta u_x \end{pmatrix} = \begin{pmatrix} \hat{c} \\ \hat{p} \\ \hat{u} \end{pmatrix} e^{i(\mathbf{q}\cdot\mathbf{r} - \omega t)}, \quad (\text{S4})$$

in the direction transverse to the ordering direction, therefore $\delta p_x = 0$. The system is linearly unstable for $\text{Im}(\omega) > 0$ and stable otherwise. The linearised system obtained from the full hydrodynamic equations is

$$\partial_t\phi_{\mathbf{q}}(t) + \mathbf{M}(\mathbf{q}) \cdot \phi_{\mathbf{q}}(t) = 0, \quad (\text{S5})$$

where

$$\mathbf{M}(\mathbf{q}) = \begin{pmatrix} iv_1 p_0 q_x + Dq^2 & iv_1 c_0 q_y & 0 \\ i\Gamma E q_y & iv_0 p_0 q_x + \Gamma K q^2 & \frac{ip_0}{q_y}(\lambda_+ q_x^2 - \lambda_- q_y^2) \\ \left(\lambda_- E p_0 q_y^2 + \frac{i\lambda a'(c_0)p_0^2 q_y^2 q_x}{q^2}\right)/\rho & ip_0 K q_y(\lambda_+ q^2 - \lambda q_y^2)/\rho & \mu q^2/\rho \end{pmatrix}. \quad (\text{S6})$$

* perlekar@tifrh.res.in

For pure bend modes ($q_x = q$, $q_y = 0$), the concentration decouples from velocity and order parameter, thus rendering the system stable. For pure splay modes ($q_x = 0$, $q_y = q$), $\mathbf{M}(\mathbf{q})$ reduces to

$$\begin{pmatrix} Dq^2 & iv_1c_0q & 0 \\ i\Gamma E q & \Gamma K q^2 & -ip_0\lambda_- q \\ \lambda_- E p_0 q^2 / \rho & -ip_0 K \lambda_- q^3 / \rho & \mu q^2 / \rho \end{pmatrix}. \quad (\text{S7})$$

The characteristic equation for the above matrix is a cubic polynomial in ω ,

$$\begin{aligned} i\omega^3 - \omega^2 q^2 \left(D + \Gamma K + \frac{\mu}{\rho} \right) - i\omega \left[\Gamma E v_1 c_0 q^2 + q^4 \left(\frac{\lambda_-^2 p_0^2 K + \mu D + \Gamma K \mu + \Gamma K D \rho}{\rho} \right) \right] \\ + \frac{\Gamma E v_1 c_0 q^4}{\rho} \left(\frac{\lambda_-^2 p_0^2}{\Gamma} + \mu \right) + \frac{q^6}{\rho} (\lambda_-^2 p_0^2 K D + \Gamma K D \mu) = 0. \end{aligned} \quad (\text{S8})$$

The roots of the above equation are

$$\begin{aligned} \omega_1 &= \frac{-iq^2(\mu + \rho D + \Gamma K \rho)}{3\rho} + \frac{i}{3 \times 2^{1/3} \rho} (A_- - A_+) \\ \omega_{2,3} &= \frac{-iq^2(\mu + \rho D + \Gamma K \rho)}{3\rho} - \frac{i}{6 \times 2^{1/3} \rho} (A_- - A_+) \pm \frac{\sqrt{3}}{6 \times 2^{1/3} \rho} (A_- + A_+) \end{aligned} \quad (\text{S9})$$

where we have defined

$$\begin{aligned} A_{\pm} &= \left(\sqrt{4B^3 + C^2} \pm C \right)^{1/3}, \text{ with} \\ B &= 3\Gamma E v_1 c_0 \rho^2 q^2 + q^4 \left(-(\mu + \rho D + \Gamma K \rho)^2 + 3\rho K \lambda_-^2 p_0^2 + 3\rho(\mu D + \Gamma K \mu + \Gamma K \rho D) \right), \text{ and} \\ C &= 9q^4 \rho^2 E v_1 c_0 (3\lambda_-^2 p_0^2 + \Gamma(2\mu - \rho D - \Gamma K \rho)) \\ &\quad + q^6 (2\mu^3 - 3(D + \Gamma K)\mu^2 \rho - 3(D - \Gamma K)^2 \mu \rho^2 + 6D\Gamma K \mu \rho^2 + 3(D^3 + \Gamma^3 K^3)\rho^3 - (D + \Gamma K)^3 \rho^3). \end{aligned}$$

In the hydrodynamic limit ($q \rightarrow 0$), expanding A_{\pm} gives,

$$A_{\pm} = 2^{1/3} \rho \left(q \sqrt{3\Gamma E v_1 c_0} \pm \frac{(3\lambda_-^2 p_0^2 + \Gamma(2\mu - \rho D - \Gamma K \rho))}{2\Gamma} q^2 \right) + \mathcal{O}(q^3). \quad (\text{S10})$$

The above expansion of A_{\pm} is valid for

$$q \ll \frac{2\sqrt{\Gamma^3 \rho^2 E v_1 c_0}}{\sqrt{3} [3\lambda_-^2 p_0^2 + \Gamma(2\mu - \rho D - \Gamma K \rho)]}.$$

Substituting Eq. (S10) in Eq. (S9) gives one stable mode,

$$\omega_1(q) = -iq^2 \left(\frac{\lambda_-^2 p_0^2}{\Gamma \rho} + \frac{\mu}{\rho} \right) + \mathcal{O}(q^3), \quad (\text{S11})$$

and two unstable modes with equal growth rates,

$$\begin{aligned} \omega_{2,3} &= \pm q \sqrt{\Gamma E v_1 c_0} - \frac{iq^2(\mu + \rho D + \Gamma K \rho)}{3\rho} + \frac{iq^2}{6\Gamma \rho} (3\lambda_-^2 p_0^2 + \Gamma(2\mu - \rho D - \Gamma K \rho)) + \mathcal{O}(q^3) \\ &= \pm q \sqrt{\Gamma E v_1 c_0} + \frac{iq^2}{2} \left[\frac{\lambda_-^2 p_0^2}{\Gamma \rho} - (D + \Gamma K) \right] + \mathcal{O}(q^3). \end{aligned} \quad (\text{S12})$$

$\omega_{2,3}(q)$ are unstable provided $\Gamma \rho (D + \Gamma K) < \lambda_-^2 p_0^2$. It is important to note that E , v_1 do not appear in $\mathcal{O}(q^2)$ term because of cancellations, but they are crucial for the instability to survive. Further, viscosity μ also cancels out in $\mathcal{O}(q^2)$ term, thus the growth rate is independent of μ in $q \rightarrow 0$ limit. On rescaling the length by $\mathcal{L} = \mu / \rho \sqrt{\Gamma E v_1 c_0}$ and time by $\mathcal{T} = \mu / \rho (\Gamma E v_1 c_0)$, we obtain the following dimensionless form of the dispersion relation which does not have explicit E dependence (see Fig. S1(b)).

$$W_{2,3} = \pm Q + \frac{iQ^2}{2} \left(\frac{\lambda_-^2 p_0^2}{\Gamma \rho} - (D + \Gamma K) \right) + \mathcal{O}(Q^3), \quad (\text{S13})$$

where $W_{2,3} = \mathcal{T} \omega_{2,3}$ and $Q = \mathcal{L} q$. Note that the above expression does not depend explicitly on E . In Fig. S1, we plot the growth rate for different E .

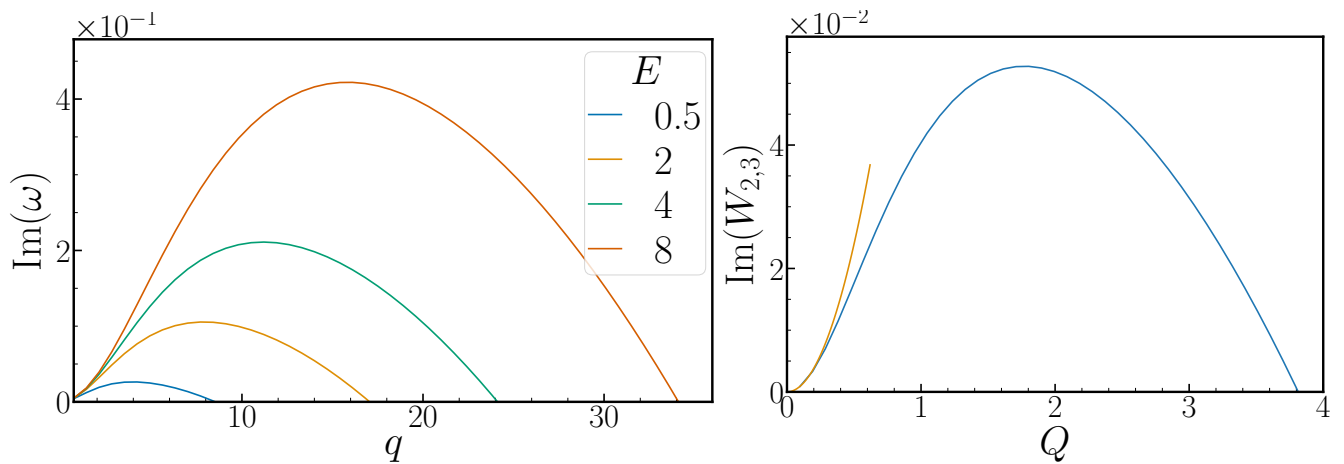


FIG. S1. (a) Dispersion curves for different E for pure splay modes. $\rho = 1$, $\mu = 0.1$, $\Gamma = 1$, $D = 10^{-4}$, $K = 10^{-3}$, $\lambda = 0.1$, $v_1 = v_0 = 0.1$, $p_0 = \sqrt{0.1}$, and $c_0 = 1$. (b) Dimensionless dispersion relation $\text{Im}(W_{2,3})$ versus Q for pure splay.

II. NUMERICAL INTEGRATION OF THE 1D EQUATION AND PEARSON'S CORRELATION

We numerically integrate the 1D equations given in the main text, reproduced here on a 1D domain of length $L = 10\pi$ and discretize it using $N = 1024$ equispaced collocation points.

$$\begin{aligned}
 \rho \partial_t v &= \mu \partial_y^2 v + \lambda_- p_0 E \partial_y^2 c, \\
 \partial_t p &= \lambda_- p_0 \partial_y v - \Gamma b p^3 + \Gamma K \partial_y^2 p - \Gamma E \partial_y c, \text{ and} \\
 \partial_t c &= -v_1 \partial_y (pc) + D \partial_y^2 c.
 \end{aligned}
 \tag{S14}$$

The time marching is performed using a second-order Adams-Bashforth scheme, and we employ a fourth-order centered finite-difference scheme for spatial derivatives. The other parameters of our simulation are $E = 0.2$, $\rho = 1$, $\mu = 0.1$, $\Gamma = 1$, $D = 10^{-4}$, $K = 10^{-3}$, $\lambda = 0.1$, $v_1 = 0.1$, and $c_0 = 1$.

Pearson's correlation for the velocity $v(y, t)$ and concentration field $c(y, t)$ is defined as [1]

$$r(t) = \frac{\sum_{i=1}^N [v(y_i, t) - \overline{v(y_i, t)}] [c(y_i, t) - \overline{c(y_i, t)}]}{\sqrt{\sum_{i=1}^N [v(y_i, t) - \overline{v(y_i, t)}]^2 \sum_{i=1}^N [c(y_i, t) - \overline{c(y_i, t)}]^2}},
 \tag{S15}$$

where the subscript i denotes the value of the field at a collocation point in the simulation domain, and $\overline{(\cdot)}$ denotes spatial averaging.

III. DISPERSION FOR THE TRAVELING WAVES

In Fig. S2, we plot the dispersion $\omega(q)$ for concentration waves in the steady state for $E = 0.15$. In this regime, we observe soliton-like waves traveling in the direction $-\nabla c/|\nabla c|$, orthogonal to each other (see Fig. 4 in the main text). The dispersion correctly captures the speed of the waves $U_E \sim \sqrt{\Gamma E v_1 c_0}$.

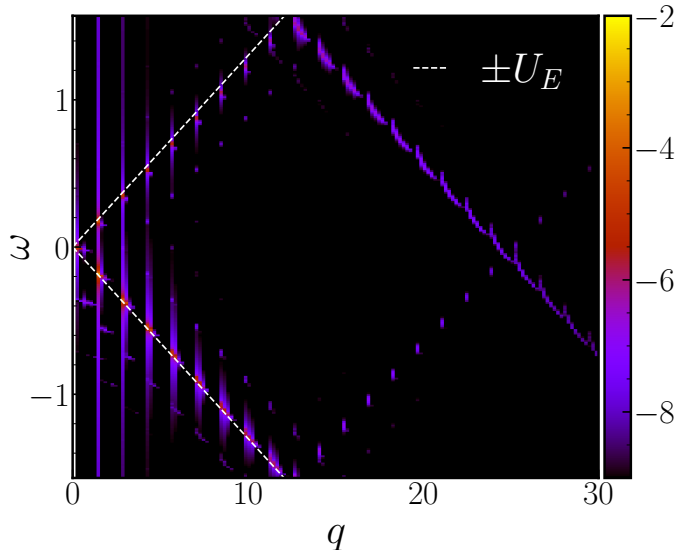


FIG. S2. Dispersion for traveling concentration waves for $E = 0.15$ in the steady state. The slopes (dashed white lines) indicates the speed of traveling waves $= \pm U_E$.

IV. CROSSOVER-PHASE

In crossover-phase ($0.8 < E < 4$), there are large fluctuations in the concentration field. In Fig. S3, we plot the time evolution of spatial variance of the concentration field as defined in the main text and typical realizations of the order parameter and the concentration fields at a given instance in time.

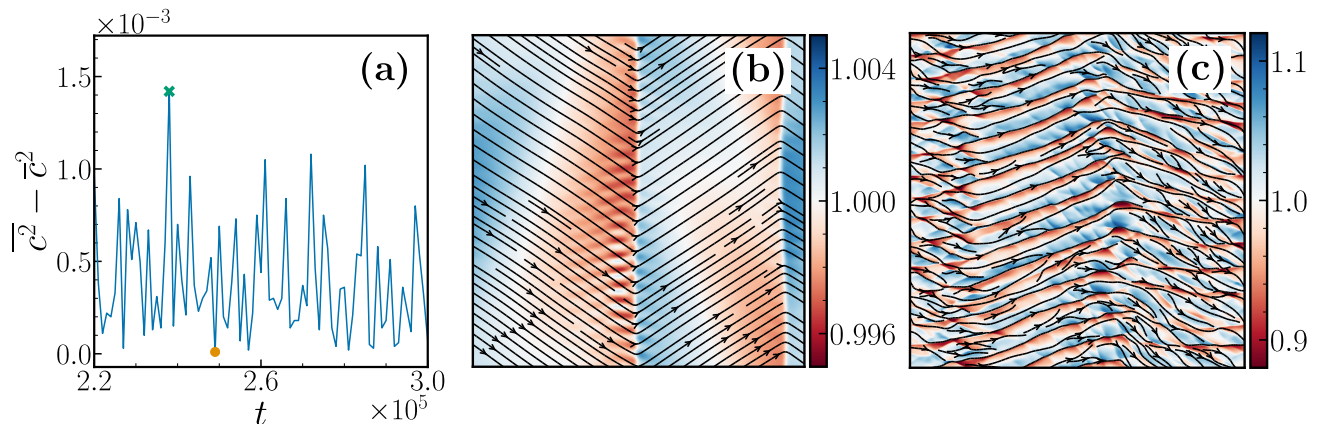


FIG. S3. Regime II: $E = 1$ (a) Time evolution of $\overline{c^2} - \bar{c}^2$ in the steady state. Pseudocolor plot of concentration overlaid with \mathbf{p} streamlines for $\overline{c^2} - \bar{c}^2 = 10^{-5}$ [(b), orange dot in (a)], and $\overline{c^2} - \bar{c}^2 = 1.4 \times 10^{-3}$ [(c), green cross in (a)].

V. CORRELATION DIMENSION

Following Rana *et al.* [2], we locate the cores of topological defects with charge +1 and analyze their spatial distribution. A uniform distribution of defects in two dimensions leads to the Porod's scaling $\mathcal{E}_p(q) \sim q^{-3}$ [2, 3]. However, we find that the topological defects show signs of clustering (see Fig. S4), which modifies the Porod's law [2]. To this extent, we calculate the correlation dimension d_2 from the spatial distribution of the defects. To find d_2 , we compute the probability of finding two defects separated by distance r , $p(r) = \int_0^r sg(s)ds$, where $g(r)$ is the radial distribution function. The scaling exponent of $p(r)$ with r determines d_2 , i.e. $p(r) \sim r^{d_2}$ [4, 5]. We find that $d_2 = 1.35$ for $\ell_E < r < \ell_*$, which yields the modified Porod's scaling $\mathcal{E}_p(q) \sim q^{-(d_2+1)} = q^{-2.35}$. For $r \gg \ell_*$, $d_2 \simeq 2$.

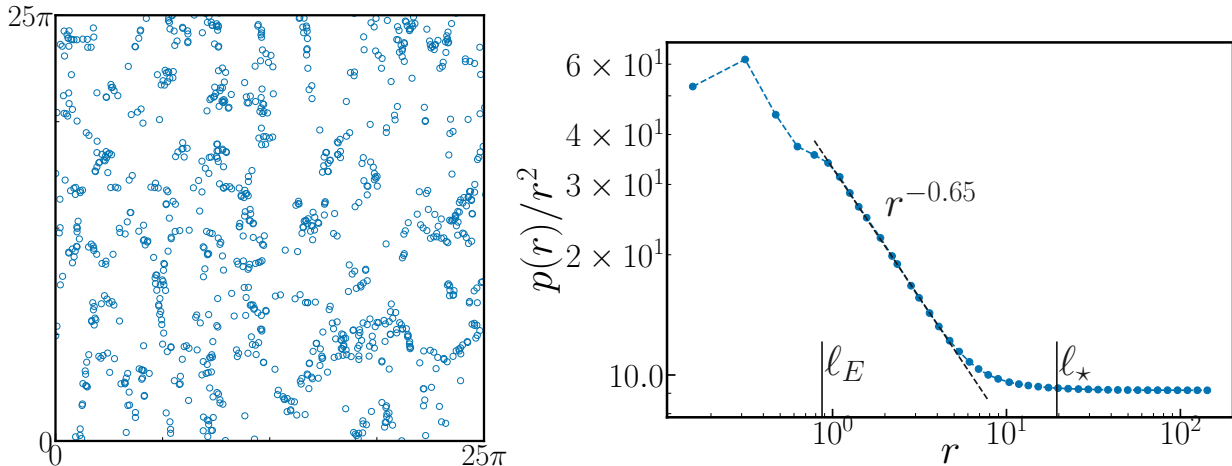


FIG. S4. (Left) Scatter plot of the cores of topological defects showing clustering at small length scales. (Right) Compensated plot of the cumulative radial distribution function $p(r)$ (scaled by r^2) shows a scaling $\sim r^{-0.65}$ in the intermediate regime $\ell_E < r < \ell_*$, which implies $d_2 = 1.35$.

VI. DESCRIPTION OF THE MOVIES

- **01.Instability_mechanism_1D.mp4** – Instability Mechanism
The movie shows the initial time evolution of concentration and velocity fields for the 1D minimal model. It emphasizes the inertia induced temporal lag, that is crucial for the instability. The two waves go out of phase occasionally which leads to the growth of the perturbations making the system unstable. The parameters are $L = 10\pi$, $N = 1024$, and $E = 0.2$.
- **02.Traveling_waves_evolution.mp4** and **03.Traveling_waves_gradient_c.mp4** – Traveling waves regime ($E = 0.15$)
02.Traveling_waves_evolution.mp4 shows time evolution of the concentration field superimposed with streamlines of \mathbf{p} . It shows two waves passing through each other without distorting their profiles. One of the waves is identified by $\nabla c \cdot \hat{\mathbf{y}} > 0$. It moves in the direction $-\nabla c/|\nabla c|$ as shown in the movie **03.Traveling_waves_gradient_c.mp4**.
- **04.Crossover_phase.mp4** – Crossover phase regime ($E = 1$).
In this regime, the streamlines of \mathbf{p} are mostly ordered with spontaneous appearance and disappearance of vortical structures with a background of concentration waves.
- **05.Concentration_wave_turbulence.mp4** – Concentration-wave turbulence ($E = 4$)
It shows the time evolution of the concentration field. We only plot a square subdomain of length 4π for clarity. Traveling concentration waves similar to regime I can be seen criss-crossing. On larger scales, the streamlines of \mathbf{p} show complex spatio-temporal structures as seen in ($E = 4$) snapshot in the main text.

-
- [1] W. H. Press, S. A. Teukolsky, W. T. Vetterling, and B. P. Flannery, *Numerical Recipes 3rd Edition: The Art of Scientific Computing*, 3rd ed. (Cambridge University Press, 2007).
 - [2] N. Rana, R. Chatterjee, S. Ro, D. Levine, S. Ramaswamy, and P. Perlekar, Defect turbulence in a dense suspension of polar, active swimmers (2023), arXiv:2305.15197 [cond-mat.soft].
 - [3] A. J. Bray, *Advances in Physics* **51**, 481 (2002).
 - [4] P. Grassberger and I. Procaccia, *Physica D: Nonlinear Phenomena* **9**, 189 (1983).
 - [5] D. Mitra and P. Perlekar, *Phys. Rev. Fluids* **3**, 044303 (2018).